

The *HST* large programme on NGC 6752 – III.

Detection of the peak of the white dwarf luminosity function

L. R. Bedin¹,¹★ M. Salaris,² J. Anderson,³ M. Libralato¹,³ D. Apai,^{4,5} D. Nardiello¹,⁶
 R. M. Rich¹,⁷ A. Bellini,³ A. Dieball,⁸ P. Bergeron,⁹ A. J. Burgasser¹,¹⁰
 A. P. Milone¹,⁶ and A. F. Marino¹,⁶

¹INAF – Osservatorio Astronomico di Padova, Vicolo dell’Osservatorio 5, I-35122 Padova, Italy

²Astrophysics Research Institute, Liverpool John Moores University, 146 Brownlow Hill, Liverpool L3 5RF, UK

³Space Telescope Science Institute, 3800 San Martin Drive, Baltimore, MD 21218, USA

⁴Department of Astronomy and Steward Observatory, The University of Arizona, 933 N. Cherry Avenue, Tucson, AZ 85721, USA

⁵Lunar and Planetary Laboratory, The University of Arizona, 1640 E. University Blvd., Tucson, AZ 85721, USA

⁶Dipartimento di Fisica e Astronomia ‘Galileo Galilei’, Università di Padova, Vicolo dell’Osservatorio 3, I-35122 Padova, Italy

⁷Department of Physics and Astronomy, UCLA, 430 Portola Plaza, Box 951547, Los Angeles, CA 90095-1547, USA

⁸Argelander Institut für Astronomie, Helmholtz Institut für Strahlen-und Kernphysik, University of Bonn, D-53121, Germany

⁹Département de Physique, Université de Montréal, C.P. 6128, Succ. Centre-Ville, Montréal, Québec H3C 3J7, Canada

¹⁰Center for Astrophysics and Space Science, University of California San Diego, La Jolla, CA 92093, USA

Accepted 2019 July 12. Received 2019 June 20; in original form 2019 March 28

ABSTRACT

We report on the white dwarf (WD) cooling sequence of the old globular cluster NGC 6752, which is chemically complex and hosts a blue horizontal branch. This is one of the last globular cluster WD cooling sequences accessible to imaging by the *Hubble Space Telescope*. Our photometry and completeness tests show that we have reached the peak of the luminosity function of the WD cooling sequence, at a magnitude $m_{F606W} = 29.4 \pm 0.1$, which is consistent with a formal age of ~ 14 Gyr. This age is also consistent with the age from fits to the main-sequence turn-off (13–14 Gyr), reinforcing our conclusion that we observe the expected accumulation of WDs along the cooling sequence.

Key words: white dwarfs – globular clusters: individual: NGC 6752.

1 INTRODUCTION

Over 97 per cent of stars end their lives as white dwarfs (WDs). The WD cooling sequence (CS) of a globular cluster (GC) is shaped by age and star formation history of that cluster, and provides a unique opportunity to conduct a census of its already evolved massive star population. WD CSs in old stellar populations can also provide critical information on how the chemical composition of a stellar remnant influences its thermal evolution.

For the oldest stellar populations, the WD CS lies in the faintest and largely unexplored regions of the colour–magnitude diagram (CMD). Deep imaging with the *Hubble Space Telescope* (*HST*) has for the first time reached the peak of the luminosity distribution of the WD CS in three *classical* GCs, namely: NGC 6397, M4, and 47 Tucanae (Anderson et al. 2008b; Bedin et al. 2009; Kalirai et al. 2012), and has revealed an unexpectedly complex, and double-peaked, WD CS in the metal-rich old open cluster NGC 6791 (Bedin et al. 2005a, 2008a,b). Each of the studied GCs hosts multiple stellar populations (mPOPs) and they show small mean spreads of

the initial He abundances (Milone et al. 2018). Their WD CSs are consistent with predictions for single-population systems (Richer et al. 2013; Campos et al. 2016).

One more *HST* investigation of WD CSs is in progress on the massive GC ω Centauri (ω Cen), where at least 15 subpopulations are known to exist (Bellini et al. 2017). The massive ω Cen has also long been known to host mPOPs, with a large spread in both [Fe/H] and (important for that investigation) initial helium abundance, as deduced from its divided main sequence (MS; Bedin et al. 2004; King et al. 2012). The upper part of the WD CS in ω Cen bifurcates into two sequences (Bellini et al. 2013): a blue CS consisting of standard CO core WDs, and a red CS consisting of low-mass WDs with both CO and He cores. The current hypothesis is that the blue WD CS is populated by the end products of the He-normal stellar population of ω Cen, while the red WD CS is populated by the end products of the He-rich population. Observing the WD CS down to the peak of its luminosity distribution provides a critical test of this hypothesis, and a resolution of the origin of the multiple WD CSs observed. That object can help to answer to key questions about He dependence in the evolution of WDs. Fortunately, ω Cen is close enough that its entire WD CS is within the reach of *HST*, and it is the subject of an investigation in progress (GO 14118+14662,

* E-mail: luigi.bedin@inaf.it

PI: Bedin; Milone et al. 2017; Bellini et al. 2018; Libralato et al. 2018).

While almost every GC is known to host multiple populations, every single cluster is unique. The GC NGC 6752 represents a transition between the relatively simple GCs, and ω Cen, the most complex GC known. NGC 6752 has an extended blue horizontal branch, a collapsed core, and three chemically distinct populations (Milone et al. 2010, 2013). It is one of our final opportunities with *HST* to increase the diversity in our very limited sample of WD CSs, thus far containing only three GCs, one old open cluster, and the complex ω Cen system. While the imminent *James Webb Space Telescope* will also be able to observe the faintest WDs in closest GCs in the infrared (IR), currently, there is no foreseeable opportunity in the post-*HST* era to observe WD CSs in the homogeneous optical photometric system of *HST*.

2 OBSERVATIONS

All images for this study were collected with the Wide Field Channel (WFC) of the Advanced Camera for Surveys (ACS) of the *HST* in program GO-15096 (PI: Bedin). Unfortunately, five out of the planned 40 orbits failed because of poor guide star acquisition and will be re-observed at a later time (currently scheduled for 2019 August). Usable data were collected between 2018 September 7 and 18, and consist of deep exposures of 1270 s each, 19 in the *F814W* filter, and 56 in *F606W*. At the beginning of each orbit shallow images, of ~ 45 s each, were also collected, in total 27 in *F606W* and only 10 in *F814W*. Note that this is an astrometric multicycle programme, and a second epoch (also of 40 orbits) has already been approved (GO-15491) and is currently scheduled for late 2020. Proper motions will eventually provide a near perfect decontamination of NGC 6752 members from field objects that are both in the foreground and background of the cluster.

Paper I of this series (Bedin et al. 2019, hereafter Paper I) presented the discovery of a serendipitous dwarf galaxy in the main studied field, while Paper II (Milone et al. 2019, hereafter Paper II) focused on multiple stellar populations detected on the low MS of NGC 6752 in our parallel observations with the IR channel of the Wide Field Camera 3 (WFC3).

3 DATA REDUCTION AND ANALYSIS

All images were pre-processed with the pixel-based correction for imperfections in the charge transfer efficiency (CTE) with methods similar to those described in Anderson & Bedin (2010). Photometry and relative positions were obtained with the software tools described by Anderson et al. (2008a). In addition to solving for positions and fluxes, important diagnostic parameters were also computed, such as the image-shape parameter (RADXS; introduced in Bedin et al. 2008a), which quantifies the fraction of light that a source has outside the predicted point spread function (PSF), the local sky noise (rmsSKY; Bedin et al. 2009), and the level of crowding (O; Anderson et al. 2008a). The RADXS parameter is useful for eliminating most of the faint unresolved galaxies that tend to plague studies of faint point sources, while the ‘O’ parameter tells how much of the flux within the PSF fitting radius comes from detected and modelled neighbours with respect to the target source. The parameter rmsSKY has a minor role in selection of sources, however, it contains precious information on how suitable the surroundings of each source are for accurate recovery and photometry.

The astrometry was registered to International Celestial Reference System (ICRS) using sources in common with *Gaia* Data Release 2 (DR2; Gaia Collaboration et al. 2018) with tabulated proper motions transformed to the epoch 2018.689826 of *HST* data, following the procedures in Bedin & Fontanive (2018).

The photometry from shallow exposures was linked to that from deep images. The photometry was calibrated on the ACS/WFC Vega-mag system following the procedures given in Bedin et al. (2005b) using encircled energy and zero-points available at Space Telescope Science Institute (STScI).¹ Finally, we applied shifts of the order of ~ 0.02 mag to link our photometry to the *state of the art* *HST* photometric catalogue by Nardiello et al. (2018) in *F606W* and *F814W*, which is obtained for a different field centred on the core of the cluster (Sarajedini et al. 2007). This registration is important as it enables us to have in the same system a better populated upper part of the CMD. For these calibrated magnitudes we will use the symbols m_{F606W} and m_{F814W} .

Artificial star tests (ASTs) have a fundamental role in this investigation, as they are used to estimate the completeness level, the errors, to optimize selection criteria, and to detect the presence of systematic errors. We performed ASTs by adding artificial stars to the individual images as described in Anderson et al. (2008a), with a random flat spatial distribution, a flat luminosity distribution in m_{F814W} between magnitude 24 and 30, and with colours chosen to place them along the observed WD CS (a fiducial line defined by hand). Indeed, following the prescriptions in Bedin et al. (2009, section 2.3), we used ASTs to perform an *input–output correction*, i.e. to correct the difference between the inserted and recovered values of magnitudes of artificial stars, a well-known systematic error (often referred to as *stellar migration*) that tends to increasingly overestimate the fluxes of stars towards fainter magnitudes. Basically, stars landing on positive peaks of noise are preferentially detected but also recovered systematically brighter (as much as ~ 0.2 mag). Hereafter, our magnitudes for both real and artificial stars are intended as corrected for such effects.

The software presented in Anderson et al. (2008a) also corrects for distortion in all the images and transforms their coordinates to a common reference frame after removal of cosmic rays and most of the artefacts. It then combines them to produce stacked images that, at any location, give the sigma-clipped mean of the individual values of pixels of all images at that location. In Fig. 1, we show a pseudo-trichromatic stack of the ACS/WFC field of view (FoV). [Note that we adopted the *F814W* images for the red channel, the *F606W* images for the blue channel, and computed a wavelength weighted (blue/red ~ 3) average of the two for the green channel.] As part of this work, we made this image publicly available (with WCS header linked to *Gaia* DR2) as supplementary online electronic material.

4 THE COLOUR–MAGNITUDE DIAGRAM

In this section, we demonstrate that we have confidently detected a sharp peak in the observed luminosity function (LF) of the WD CS, which we will show in the next sections to be consistent with the peak of the CO WD luminosity distribution in NGC 6752.

In order to detect the faintest sources we allow our algorithms to find any local maximum with a non-null flux in both filters above the local sky, as a potential real object. In principle, one every 9 pixels could generate such a peak, we ended up with ‘just’ $\sim 162\,000$ local

¹<http://www.stsci.edu/hst/acs/analysis/zeropoints>

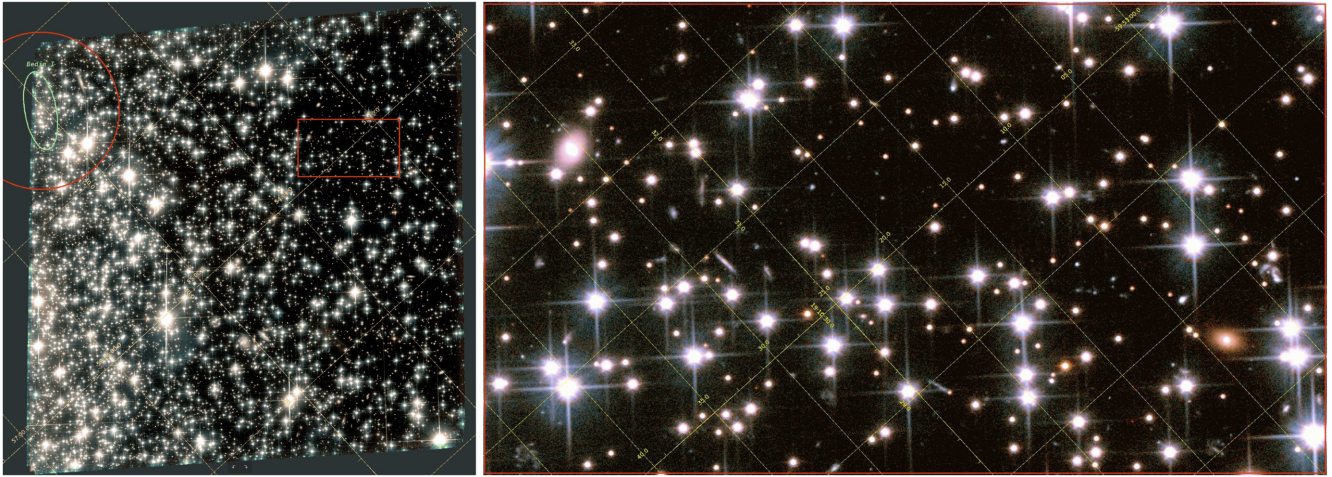


Figure 1. Left: trichromatic view of the entire ACS/WFC field of the *HST* program GO-15096. Note the relatively high gradient in stellar density. Yellow grids give coordinates for the ICRS. The green ellipse indicates the Bedin I dwarf galaxy, and the red circle the region masked out as potentially contaminated by the dwarf galaxy. Right: zoom-in of the area indicated with a red rectangular in the left-hand panel. This being representative of the regions with the lowest sky brightness in the field.

maxima, or one every $\sim 10 \times 10$ pixel². The CMD for these detected local peaks – without any selection – is shown in panel (a) of Fig. 2.

Paper I presented the discovery of a dwarf spheroidal galaxy (dSph) – designated Bedin I – in the background of NGC 6752, which is close to the upper left-hand corner of the FoV in Fig. 1. The RGB stars of this stellar system happen to contaminate the region of the CMD where WDs are located. For this reason we have chosen to completely mask out and not use any sources in the region of the FoV occupied by this resolved background dwarf galaxy. The mask is circular, centred on Bedin I, and has a radius of 800 pixels (~ 40 arcsec). We also require that any of the detected sources generates a peak in at least nine out of the 19 *F814W* images and in at least 26 out of the 56 *F606W* images. With these first selections the number of suitable peaks drops to $\sim 116\,000$, and their CMD is shown in panel (b). Still many of these peaks are artefacts and spurious detections.

Our next selection is illustrated in panel (c) and removes objects falling in the regions of the field that are too noisy to detect such objects at all. As we will see, this mild selection in rmsSKY has more significant implications when used to estimate the completeness limited to portions of the FoV suitable for actual detection of faint sources.

The most effective parameter for the selection of real point sources is RADXS (Bedin et al. 2008a, 2009, 2010, 2015). This parameter is a measure of how much flux there is in the pixels just outside of the core, in excess of the prediction from the PSF: RADXS is positive if the object is broader than the PSF, and negative if it is sharper. Even mild selection criterion imposed on this parameter is sufficient to reject 2/3 of the initially detected peaks. The result of this selection of peaks with $-0.35 < \text{RADXS} < +0.25$ is shown in panel (d).

Our last selection criterion is applied through the parameter ‘O’ (Anderson et al. 2008a), the fraction of light due to neighbours. We require that the flux of light within the PSF normalized aperture due to neighbours do not exceed four times the flux of the target source ($O < 4$). This criterion further reduces the sample by ~ 10 per cent, and the $\sim 25\,000$ surviving sources are shown in panel (e).

It is clear, however, that there is only so much we can do to optimize selection criteria parameters at the faintest end, as going

fainter, it becomes increasingly difficult to estimate the real shape of sources, or to get any meaningful intrinsic parameters at all. At this point it becomes more important to merely assess whether, and at what level, a given local peak is significant with respect to the noise of the local sky. Therefore we proceed as follows. Given that in filter *F814W* our PSFs contains ~ 16 per cent of the light in its central pixel, and about ~ 18 per cent in *F606W*, we can use the standard deviation (σ) of pixel values in empty regions of the sky to estimate the magnitude level that corresponds to 3σ and 5σ levels in the sky noise. To transform these noise levels into total flux, we divide these 3σ – 5σ by the fraction of total flux (i.e. 0.16 for *F814W* and 0.18 for *F606W*), then convert these values into instrumental magnitudes $-2.5 \log(\text{total flux})$, and finally calibrate them with ACS/WFC Vega-mag zero-points. As expected, the bulk of these peaks have white noise, and as such an instrumental colour centred at instrumental magnitudes 0.00 (or once calibrated, ~ 1 in $(m_{F606W} - m_{F814W})$).

The grey shaded areas in all panels of Fig. 2 show the regions for peaks with a significance less than 5σ , as estimated in the least noisy portion of the field (the rectangular region in red in Fig. 1). The green dotted lines instead mark the 3σ significance level. This essentially is the estimated noise floor level in the darkest portion of the FoV. Hereafter, we choose to consider all the detections below these green lines as not significant.

Panels (a’), (b’), (c’), (d’), and (e’) repeat these selections for artificial stars. However, there are two additional conditions for ASTs: we know where we added artificial stars, and at which magnitudes. Therefore we impose generous requirements for the recovered artificial stars. An artificial star is successfully recovered if it lies within 1 pixel from its positions in both coordinates, and within 0.75 mag from its added flux in both filters. These criteria are sufficient to remove all the potential mismatches of sources with local maxima in the noise, and that is the reason why the bulk of the noise floor level is not seen in CMDs of ASTs. These CMDs show that added stars are successfully recovered down to the estimated 3σ level.

The concept of effective (or local) completeness was first introduced in Bedin et al. (2008a), and successively used in other independent studies (Bedin et al. 2009, 2010, 2015). The idea is

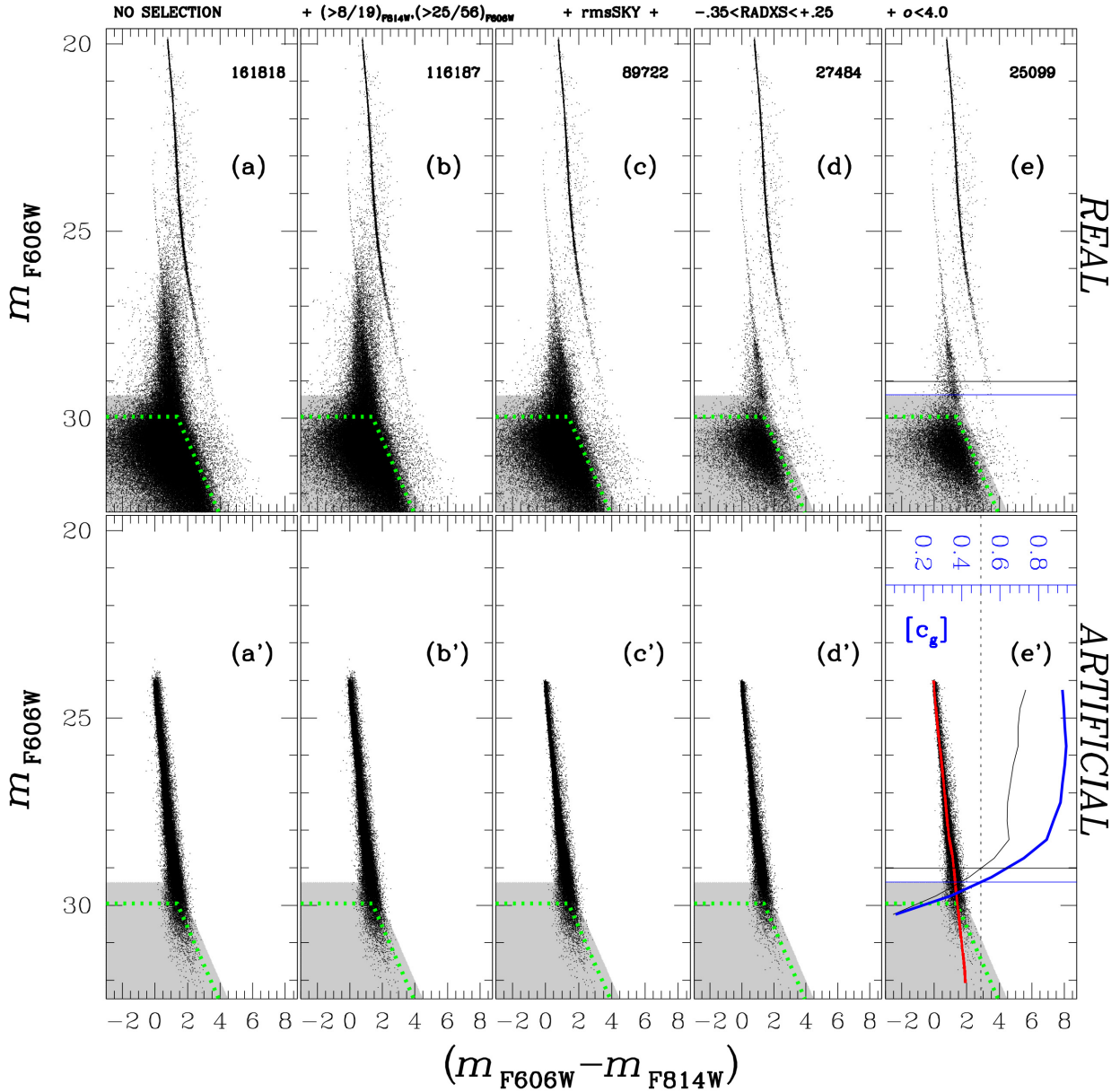


Figure 2. From left to right, the CMDs are subject to an increasing number of selection criteria (see text). Top panels refer to *real* stars while bottom panels to *artificial* stars. Panel (e') shows the traditional completeness (black line) and the effective completeness ($[c_g]$ in blue, see text), the reference scale for which is shown in blue.

simple: we cannot hope to recover faint stars around the bright haloes of saturated stars, where the shot noise is already higher than the signal from the faint sources we would hope to recover/detect. Therefore we should limit our search for faint sources to only those regions of the FoV where the sky noise is sufficiently faint to allow the faint sources to be detected.

We use ASTs to map these regions and, in practice, we limit our search for faint stars to only those regions. Naturally, if the completeness is limited to only suitable search areas that exclude the bright haloes of saturated stars (see Fig. 1), this approach improves with respect to the completeness computed for the overall field. Panel (e') also shows both the traditional (overall) completeness and the effective (local) completeness, where the top-axis (in blue) refers to completeness values. The traditional completeness is indicated with a black line, and this seems to never exceed ~ 70 per cent for

the faint magnitude range considered here. Instead, the effective completeness (blue line) can be as high as 95 per cent. Note that the ratio of the two tells us what is the usable fraction of the area to search for stars of a given magnitude.

The conventional rule of trusting only completeness down to 50 per cent would set the limit of validity of our WD CS LF study down to $m_{F606W} \simeq 29.4$. Interestingly enough, however, this is brighter than the estimated 5σ regions highlighted in grey in Fig. 2.

4.1 The observed WD CS LF of NGC 6752

Lacking proper motions until the acquisition of our second epoch, our next best option is to obtain as pure as possible a sample of NGC 6752 WD members based on their position in the CMD.

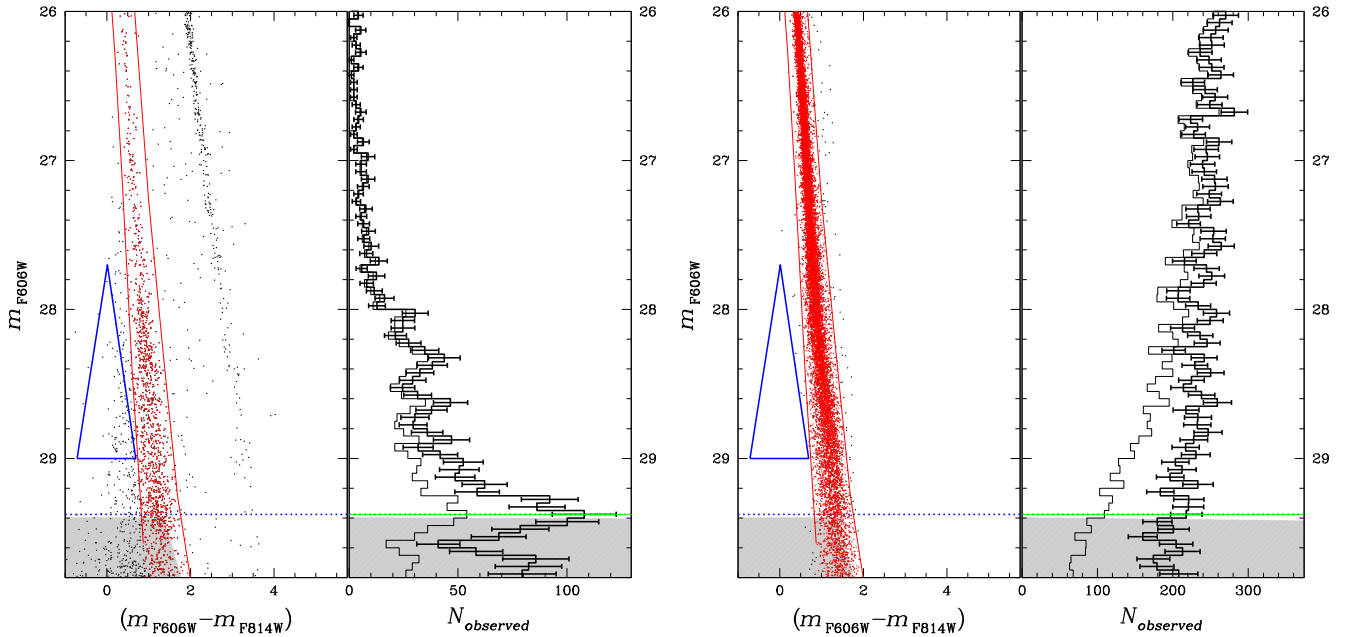


Figure 3. Left: on the left-hand panel the CMDs for selected real sources. The blue triangle indicates the region where faint blue unresolved background galaxies are expected to be; it was defined by Bedin et al. (2008a) using data from the *Hubble Ultra Deep Field*. The two red lines delimit the region of the CMDs where we assume most of WDs to be. The right-hand panel shows the observed LF for the WD candidates highlighted in red in the left-hand panel (thin histogram). The completeness-corrected WD CS LF is shown with error bars (thick line). A horizontal blue dotted line marks the 50 per cent of $[c_g]$, while the green horizontal line marks the location of the peak of the WD CS LF at $m_{F606W} = 29.375 \pm 0.100$. The grey regions indicate the 5σ threshold above the local sky, estimated for the darkest portion of the FoV. Right: same panels just for the artificial stars. Note that the two red lines encompass most of the recovered stars. The artificial stars were added along the WD CS with a flat distribution in $F814W$, which however results in a not flat distribution in $F606W$.

We do expect several field objects to fall along the WD CS locus of NGC 6752, and to affect the exact shape of the WD LF we derive here. However, we cannot foresee a scenario in which the field objects would introduce a well-defined peak mimicking that of the WD LF. In the following we will review three possible sources of contaminants (background/foreground field stars, resolved galaxies, and unresolved galaxies) and address why these sources are very unlikely to introduce the observed feature.

We tested the best available models of star distribution for Galactic *field stars* in the background and foreground of NGC 6752 (such as the Besançon models² by Robin et al. 2003) and obtained a rather flat distribution with no peaks. Only ~ 200 field stars are expected within the WD CS region between $m_{F606W} = 22$ and 29.6, compared to a total of over 1200 observed, with between 5 and 9 stars per 0.05-mag bin in the region of the WD LF peak.

Empirically, these numbers and colour–magnitude distributions of field stars are also supported by similar studies on WDs of star clusters at any height above the Galactic plane (Anderson et al. 2008b; Bedin et al. 2008a,b, 2009, 2010, 2015; Kalirai et al. 2012).

Similarly, we do not expect contamination by background galaxies to mimic the observed feature. All background galaxies sufficiently large and bright to have well established shapes (i.e. above the 5σ lines) were easily removed by the selection in the RADXS parameter (even sharp quasar-like object, at *HST* resolution, reveals departures from PSFs; e.g. Bedin et al. 2003).

A possible concern could be the contamination by faint, compact, blue, and unresolved galaxies in the background of NGC 6752.³

However, thanks to decades of deep *HST* observations their numbers and loci in the CMD are well known. For this purpose, a region in the CMD was carefully defined by Bedin et al. (2008a, 2009) and demonstrated to not overlap with the clusters WD CSs.

In Fig. 3, we show the CMDs for the selected sources defined in panels (e) and (e') of Fig. 2. Again, ASTs turn out to be very useful to define the location of reliably measured WDs along the fiducial CS of NGC 6752 for the entire magnitude range of interest. Sources between the two red lines defined by hand in the CMD for ASTs (right-hand panels) are assumed to be good WD members of NGC 6752 including photometric errors. Identical lines are also used to define the sample of WDs among real stars (left-hand panels). The blue triangle shows the location of blue-compact unresolved background galaxies adopted by Bedin et al. (2009) using *Hubble Ultra Deep Field* (HUDF) data, and transformed into the $F814W$ filter as was done in Bedin et al. (2008a). Note that the adopted WD region is not contaminated by this blue-compact galaxies triangular region; this is a conservative statement, as the lower reddening of NGC 6752 with respect to NGC 6791 would make this triangular region about 0.1 mag bluer (and so even more distant from the WD region). Note also that these selections are large enough to take into account the photometric error distributions of unresolved point sources.

On the CMD for real sources of Fig. 3, there are many sources that lie outside the red boundary that defines the WD sequence. These are the expected mixture of stars in the Galactic field, many of which are WDs. These field stars are expected to contaminate both the triangular region of the blue-compact galaxies and the WD region, therefore, they affect the exact shape of the WD LF.

We then count the observed objects (N) at the various m_{F606W} magnitudes, and correct their values for the *effective* completeness (c_g), obtaining the completeness-corrected WD LF values (N_{c_g}).

²https://model.obs-besancon.fr/modele_descrip.php

³Those not already removed by the RADXS photometric selections described in previous section.

Table 1. Completeness-corrected white dwarf luminosity function (see text). Full table available as supplementary online electronic material.

m_{F606W}	N_{c_g}	$\sigma_{N_{c_g}}$	N	$[c_g]$
24.025	1.0863	1.0863	1	0.9205
24.075	0.0000	0.0000	0	0.9212
24.125	1.0846	1.0846	1	0.9220
24.175	1.0838	1.0838	1	0.9227
24.225	1.0829	1.0829	1	0.9234
24.275	1.0821	1.0821	1	0.9242
24.325	2.1624	1.5291	2	0.9249
24.375	0.0000	0.0000	0	0.9256
24.425	2.1590	1.5266	2	0.9264
24.475	0.0000	0.0000	0	0.9271

In Table 1, we report the values of the entire WD LF and relative uncertainties. We must treat these numbers with care, however. Not only because energy equipartition is expected to cause the more massive WDs to migrate toward the centre of the cluster, but also because of unaccounted for residual contamination due to field objects or to artefacts. Nevertheless, these uncertainties can only bias the relative numbers, while the WD LF peaks at a magnitude where our completeness is still reliable, and where contaminants cannot affect its true positions.

We define the peak of the WD LF as the bin with the highest value, which is at $m_{F606W} \simeq 29.4$. As formal uncertainty we assume $\sigma = \text{FWHM}/2.354 \simeq 0.1$ mag, where FWHM is the full width at half-maximum of the peak, which is 0.2 mag. At the magnitude of the peak, we observe a rather flat distribution of field objects on the blue side of the WD CS region, at maximum ~ 20 objects bin^{-1} (completeness corrected). Assuming a similar field contamination with a similar distribution within the WD CS region (the best we can do), we do not expect the position of the peak to change.

5 THEORETICAL ASSESSMENT OF THE LF AND CONCLUSIONS

We now present the first preliminary comparison of the WD LF with models.

Future epochs will enable us to carry out an exhaustive characterization of the observed WD LF of NGC 6752 and of its exact shape, thanks to improved signal-to-noise ratio (S/N; through the doubling of the exposure time) and proper motion cleaning for artefacts and for field objects (in both the background and foreground). Indeed, the increased S/N planned for the future will enable us to study in detail not only the exact shape of the WD LF but also the exact shape of the WD CS in the CMD (Anderson et al. 2008b). Here, instead, we only aim to just verify that the rather sharp peak in the observed LF, as supported by the artificial star tests, is roughly consistent with the magnitude theoretically expected for the peak in the LF of the cluster WD CS.

As a first step we have determined the reddening and cluster distance modulus from our data, by fitting theoretical isochrones to the colour of the cluster unevolved MS between $m_{F606W} = 18$ and 21, and the red giant branch (see middle panel of Fig. 4). To this purpose we have employed our own photometry, complemented by the Nardiello et al. (2018) catalogue, which is consistent with our photometry for the common evolutionary phases. This latter catalogue includes a well-populated red giant branch, as well as the horizontal branch. Stars in this cluster display a small mean range of initial helium mass fraction ($\Delta Y = 0.015 \pm 0.005$; Nardiello et al. 2015; Milone et al. 2018; Paper II), so that we can proceed by

employing isochrones with a single initial He abundance without introducing any major bias in our analysis.

We employed the α -enhanced BaSTI (Pietrinferni et al. 2006) isochrones with $[\text{Fe}/\text{H}] = -1.6$, $Y = 0.246$, and employed the extinction law in the ACS filters determined by Bedin et al. (2005b). The isochrone metallicity is close to $[\text{Fe}/\text{H}] = -1.48 \pm 0.06$ that was determined spectroscopically by Gratton et al. (2005) for NGC 6752. The fit provides $E(B - V) = 0.05$ (consistent with $E(B - V) = 0.046 \pm 0.005$ as determined by Gratton et al. 2005) and $(m - M)_0 = 13.10$. This distance modulus compares well with $(m - M)_0 = 12.92 \pm 0.24$ obtained from the *Gaia* DR2 cluster parallax suggested by the *Gaia* Collaboration et al. (2018) after the offset correction discussed by Lindegren et al. (2018). The error on this *Gaia* distance modulus is, however, still sizable, due to the ‘calibration noise’ described by the *Gaia* Collaboration et al. (2018). The top section (1) of the right-hand panel of Fig. 4 shows that, with this distance modulus and reddening, the theoretical zero age horizontal branch sequence is also a good match to the observed counterpart (the redder part of the observed horizontal branch is populated by stars evolving to the asymptotic giant branch phase). Ages of 13 and 14 Gyr bracket the position of the age-sensitive subgiant branch in the CMD (see the middle section of the same panel). The isochrones do not include the effect of atomic diffusion. Its inclusion would decrease these ages by ~ 1 Gyr (see e.g. Vandenberg et al. 2002).

The bottom section (3) of the right-hand panel of Fig. 4 compares the observed CS with BaSTI WD isochrones (Salaris et al. 2010), shifted employing the reddening and distance modulus derived above from the main-sequence turn-off (MSTO) isochrones fit. These WD isochrones include CO separation upon crystallization by employing the Segretain & Chabrier (1993) phase diagram for the CO mixture. We have determined with appropriate calculations that the more modern Horowitz, Schneider & Berry (2010) CO phase diagram would decrease the WD cluster ages by ~ 0.9 Gyr, compared to the results reported below. We show two DA isochrones for an age of 14 Gyr, calculated with progenitor lifetimes (and CO profiles) for the same chemical composition as the MSTO isochrones. These WD isochrones cover the WD mass range from 0.54 to 1.0 M_\odot . More massive WDs between 1.0 and $\sim 1.4 M_\odot$ (if they form in metal-poor clusters) would be fainter than the faintest magnitude of our isochrones. However, for any reasonable mass function, they would constitute only a fraction of a per cent of the total cluster WD population. The first isochrone (displayed in red) has been calculated with the linear initial-final mass relationship (IFMR) from Salaris et al. (2009). The IFMR was extrapolated linearly such that initial masses typical of stars populating Galactic GC MSTO ($\sim 0.8 M_\odot$) produce WDs with mass 0.54 M_\odot (this IFMR was determined down to values of initial masses $\sim 1.8 M_\odot$). This mass is consistent with the observational analysis of Kalirai et al. (2009), who show that bright WDs in the Galactic GC M 4 are generally of DA type, with a typical mass equal to $0.53 \pm 0.01 M_\odot$ (we denote this isochrone as *isochrone A*).

The second DA isochrone (displayed as blue solid line in the figure) is calculated by extrapolating Salaris et al. (2009) IFMR to reach a WD mass equal to 0.49 M_\odot for initial masses below 1.0 M_\odot (we denote this isochrone as *isochrone B*). The reason for this choice is that, as derived from the detailed horizontal branch modelling by Cassisi et al. (2014), a fraction of the stars populating this cluster’s blue horizontal branch have a mass close to the core mass at the He-flash for this metallicity (equal to $\sim 0.49 M_\odot$). They will evolve straight to the WD phase skipping the asymptotic giant branch.

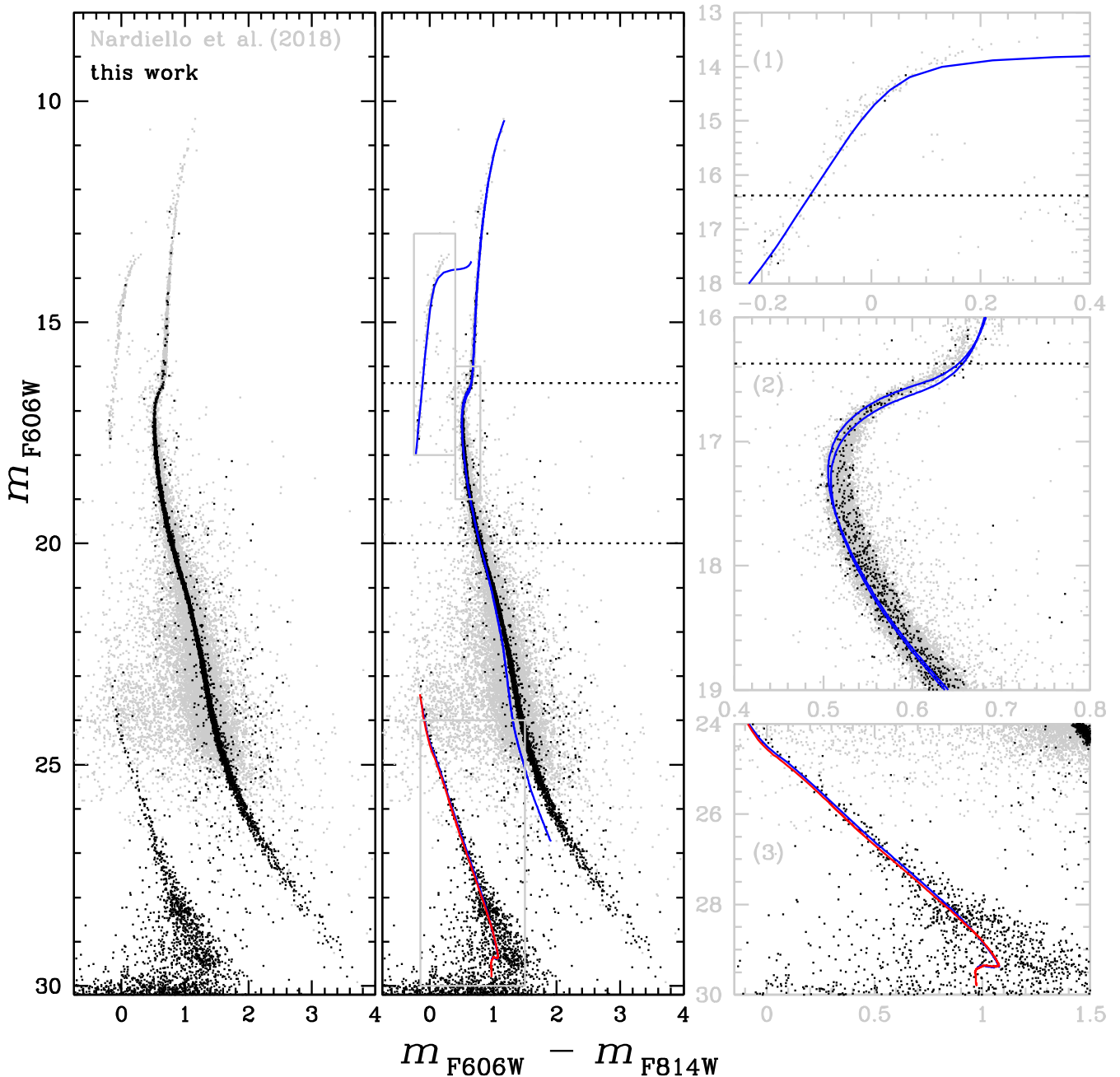


Figure 4. Left: entire CMD of NGC 6752, including main sequence (MS), subgiant, red giant, horizontal branches, and WDs. Black dots denote our photometry, while grey dots the Nardiello et al. (2018). Middle: the same CMD, where solid lines display: isochrones for 13 and 14 Gyr for the main-sequence turn-off (MSTO), two 14 Gyr DA WD isochrones, and the theoretical zero age horizontal branch, all shifted by $E(B - V) = 0.05$ and $(m - M)_0 = 13.10$ (see text for details). In this panel the horizontal dotted lines mark where saturation start in our deep and short exposures. Right: zoom-in of the three grey regions defined in the middle panel [and labelled as (1), (2), and (3)] to highlight the comparison of observations with theory in the different evolutionary phases.

Isochrones A and B differ only at magnitudes brighter than $m_{F606W} \sim 29.0$, where the CS is populated by fast evolving WDs produced by stars that have just left either the horizontal branch, or the post-asymptotic giant branch phase. Overall, the observed CS is closely matched by the theoretical isochrones at magnitudes brighter than $m_{F606W} \sim 28.2$, which however progressively diverge towards bluer colours with increasing magnitudes.

Fig. 5 compares the empirical (completeness corrected) WD LF with two theoretical LFs determined from the two 14 Gyr old DA

WD isochrones of Fig. 4. Random photometric errors were added to stars, following the results of the artificial star tests, and shifted by the derived extinction and distance modulus.

The total number of stars in the theoretical LFs has been chosen to approximately match the value of the peak of the observed LF at $m_{F606W} \sim 29.4$, employing a WD progenitor mass function as a power law with exponent -1.9 . This exponent was selected to match approximately the observed star counts at least at another magnitude level ($m_{F606W} \sim 28.8$), in addition to the peak at

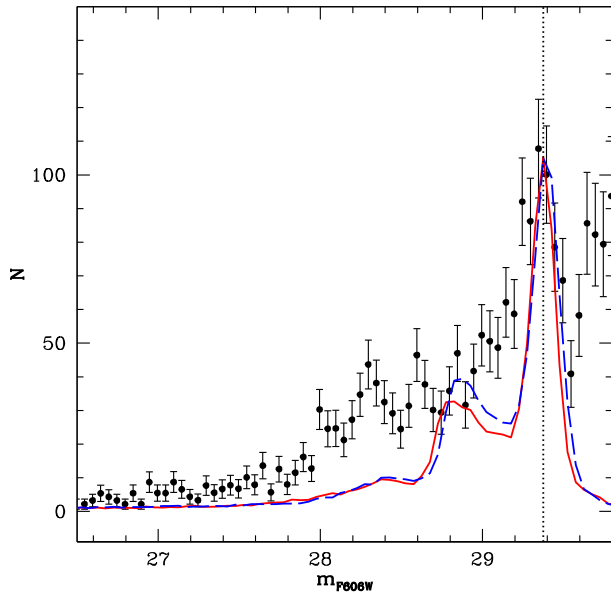


Figure 5. Observed (completeness corrected) WD LF (filled circles with error bars), together with two different theoretical LFs (red solid and blue dashed lines) for an age of 14 Gyr, shifted by our derived cluster distance modulus and extinction. The solid line corresponds to the LF calculated with isochrone A of Fig. 4, whilst the dashed line corresponds to calculations employing isochrone B in the same figure. The dotted vertical line marks the magnitude level of the 50 per cent completeness threshold.

$m_{F606W} \sim 29.4$. Varying the exponent of the progenitor mass function alters the shape of the theoretical LF, but not the brightness of its peak.

The two different IFMRs employed for isochrones A and B produce identical LFs at the faint parts of the CS. This is not surprising given that the main difference is the value of the initial mass only for low-mass progenitors.

An exhaustive comparison of observed versus theoretical LFs must wait for future epochs that will enable to *clean* the cluster WD sample more reliably. As things stand, irrespective of the choice of the progenitor mass function exponent, the theoretical LFs cannot match the observed LF along the entire CS. The purpose of this comparison is therefore just qualitative, but it serves to highlight the fact that the magnitude level of the predicted peak of the WD LF does match the magnitude of the observed LF peak, when an age consistent with the cluster turn-off age is employed.

This strengthens the case for our detection of the peak in the WD LF of NGC 6752.

ACKNOWLEDGEMENTS

This study is based on observations with the NASA/ESA *Hubble Space Telescope*, obtained at the Space Telescope Science Institute, which is operated by AURA, Inc., under NASA contract NAS 5-26555.

JA, RMR, DA, AD, AB, and ML acknowledge support from *HST*-GO-15096. APM acknowledges funding from the European Research Council (ERC) under the European Union’s Horizon 2020 research innovation programme (Grant Agreement ERC-StG 2016, No. 716082 ‘GALFOR’). APM also acknowledges support from MIUR through the FARE project R164RM93XW ‘SEMPlice’. AFM has received funding from the European

Union’s Horizon 2020 research and innovation programme under the Marie Skłodowska-Curie Grant Agreement No. 797100. DN acknowledges partial support by the University of Padova, Progetto di Ateneo, Grant BIRD178590. This work is supported in part by the NSERC Canada (PB). LRB acknowledges support by MIUR under PRIN program #2017Z2HSMF.

REFERENCES

- Anderson J., Bedin L. R., 2010, *PASP*, 122, 1035
 Anderson J. et al., 2008a, *AJ*, 135, 2055
 Anderson J. et al., 2008b, *AJ*, 135, 2114
 Bedin L. R., Fontanive C., 2018, *MNRAS*, 481, 5339
 Bedin L. R., Piotto G., King I. R., Anderson J., 2003, *AJ*, 126, 247
 Bedin L. R., Piotto G., Anderson J., Cassisi S., King I. R., Momany Y., Carraro G., 2004, *ApJ*, 605, L125
 Bedin L. R., Salaris M., Piotto G., King I. R., Anderson J., Cassisi S., Momany Y., 2005a, *ApJ*, 624, L45
 Bedin L. R., Cassisi S., Castelli F., Piotto G., Anderson J., Salaris M., Momany Y., Pietrinferni A., 2005b, *MNRAS*, 357, 1038
 Bedin L. R., King I. R., Anderson J., Piotto G., Salaris M., Cassisi S., Serenelli A., 2008a, *ApJ*, 678, 1279
 Bedin L. R., Salaris M., Piotto G., Cassisi S., Milone A. P., Anderson J., King I. R., 2008b, *ApJ*, 679, L29
 Bedin L. R., Salaris M., Piotto G., Anderson J., King I. R., Cassisi S., 2009, *ApJ*, 697, 965
 Bedin L. R., Salaris M., King I. R., Piotto G., Anderson J., Cassisi S., 2010, *ApJ*, 708, L32
 Bedin L. R., Salaris M., Anderson J., Cassisi S., Milone A. P., Piotto G., King I. R., Bergeron P., 2015, *MNRAS*, 448, 1779
 Bedin L. R. et al., 2019, *MNRAS*, 484, L54 (Paper I)
 Bellini A., Anderson J., Salaris M., Cassisi S., Bedin L. R., Piotto G., Bergeron P., 2013, *ApJ*, 769, L32
 Bellini A., Milone A. P., Anderson J., Marino A. F., Piotto G., van der Marel R. P., Bedin L. R., King I. R., 2017, *ApJ*, 844, 164
 Bellini A. et al., 2018, *ApJ*, 853, 86
 Campos F. et al., 2016, *MNRAS*, 456, 3729
 Cassisi S., Salaris M., Pietrinferni A., Vink J. S., Monelli M., 2014, *A&A*, 571, A81
 Gaia Collaboration et al., 2018, *A&A*, 616, A1
 Gratton R. G., Bragaglia A., Carretta E., de Angeli F., Lucatello S., Momany Y., Piotto G., Recio Blanco A., 2005, *A&A*, 440, 901
 Horowitz C. J., Schneider A. S., Berry D. K., 2010, *Phys. Rev. Lett.*, 104, 231101
 Kalirai J. S., Saul Davis D., Richer H. B., Bergeron P., Catelan M., Hansen B. M. S., Rich R. M., 2009, *ApJ*, 705, 408
 Kalirai J. S. et al., 2012, *AJ*, 143, 11
 King I. R. et al., 2012, *AJ*, 144, 5
 Libralato M. et al., 2018, *ApJ*, 854, 45
 Lindegren L. et al., 2018, *A&A*, 616, A2
 Milone A. P. et al., 2010, *ApJ*, 709, 1183
 Milone A. P. et al., 2013, *ApJ*, 767, 120
 Milone A. P. et al., 2017, *MNRAS*, 469, 800
 Milone A. P. et al., 2018, *MNRAS*, 481, 5098
 Milone A. P. et al., 2019, *MNRAS*, 484, 4046 (Paper II)
 Nardiello D., Milone A. P., Piotto G., Marino A. F., Bellini A., Cassisi S., 2015, *A&A*, 573, A70
 Nardiello D. et al., 2018, *MNRAS*, 481, 3382
 Pietrinferni A., Cassisi S., Salaris M., Castelli F., 2006, *ApJ*, 642, 797
 Richer H. B. et al., 2013, *ApJ*, 778, 104
 Robin A. C., Reylé C., Derrière S., Picaud S., 2003, *A&A*, 409, 523
 Salaris M., Serenelli A., Weiss A., Miller Bertolami M., 2009, *ApJ*, 692, 1013
 Salaris M., Cassisi S., Pietrinferni A., Kowalski P. M., Isern J., 2010, *ApJ*, 716, 1241

Sarajedini A. et al., 2007, *AJ*, 133, 1658
Segretain L., Chabrier G., 1993, *A&A*, 271, L13
VandenBerg D. A., Richard O., Michaud G., Richer J., 2002, *ApJ*, 571, 487

SUPPORTING INFORMATION

Supplementary data can be found at: https://web.oapd.inaf.it/bedin/files/PAPERS_eMATERIALS/NGC6752.III/.

Table 1. Completeness-corrected white dwarf luminosity function.

Figure 1. Trichromatic view of the entire ACS/WFC field of the *HST* program GO-15096.

Please note: Oxford University Press is not responsible for the content or functionality of any supporting materials supplied by the authors. Any queries (other than missing material) should be directed to the corresponding author for the article.

This paper has been typeset from a $\text{\TeX}/\text{\LaTeX}$ file prepared by the author.